ROYAL SOCIETY OF CHEMISTRY

## PAPER

Check for updates

# Minimalist and nanoparticle-free selenium-based photocathodes for record performance solar-driven hydrogen evolution

Edoardo Maggi, [ID] *[abc] Oriol Segura-Blanch, [ID] [ac] Ivan Caño, [ID] [ac] Arnau Torrens, [ID] [ac] Alex Jimenez-Arguijo, [ID] [ac] Pau Estarlich, [ID] [a] Lorenzo Calvo-Barrio, [ID] [de] Hao Zhe Chun, [ID] [f] Mario F. Garcia-Sanchez, [ID] [g] Marcel Placidi, [ID] [ac] Joaquim Puigdollers, [ID] [ac] Jordi Llorca, [ID] [bc] Lydia Helena Wong, [ID] [f] Lluís Soler [ID] [bc] and Edgardo Saucedo [ID] [ac]

This work reports the highest photoelectrochemical (PEC) performance for selenium (Se)-based photocathodes, achieved through a simple, sustainable, and nanoparticle-free design. A half-cell solar-to-hydrogen (HC-STH) efficiency of $2.78 \pm 0.01\%$ and a photocurrent density of $11.35 \pm 0.01$ mA cm$^{-2}$ at $0$ V$_{RHE}$ were obtained with bare Mo/Se devices tested in H$_2$SO$_4$, surpassing the previous Se-based (FTO/Se/TiO$_2$/Pt) HC-STH benchmark by over a factor of seven. To improve sustainability and device safety, the deposition of a thin TiO$_2$ passivation layer enabled comparable performance ($2.76 \pm 0.01\%$), even in neutral phosphate buffer, allowing to obtain the highest photoelectrocatalytic onset potential reported so far ($0.74$ V$_{RHE}$). Unlike most PEC devices that rely on complex multilayer stacks and costly noble metals, which limit scalability and environmental compatibility, this work demonstrates that high performance can be achieved with a fully earth-abundant and low-toxicity materials set. A systematic screening of back contacts, Se phases, absorber thickness, protective overlayers, and electrolyte formulations revealed the crucial role of Mo in enhancing Se orientation, charge extraction, and photovoltage generation. These results establish multiple benchmarks for Se-based PEC water splitting and highlight the potential of streamlined and scalable architectures for efficient and sustainable green hydrogen production.

### Broader context

Photoelectrochemical (PEC) water splitting is a leading approach for sustainable hydrogen production, directly converting solar energy into chemical fuel. Developing efficient and low-cost photocathodes is essential for scaling this technology. Among the materials considered, selenium (Se) is an earth-abundant chalcogenide with a long history in optoelectronics. Its favorable conduction band position relative to the hydrogen evolution potential makes it an inherently suitable photocathode material. Unlike many complex semiconductors used in PEC, Se offers a simple elemental composition, low toxicity, and compatibility with scalable vacuum-based fabrication methods. Despite these advantages, PEC research on Se has been limited, and existing Se-based photocathodes have exhibited modest efficiencies, always requiring noble metal catalysts or multi-layered device stacks to enhance performance. In this work, we demonstrate that high-performance PEC hydrogen evolution is achievable with a minimalist, nanoparticle-free Mo/Se architecture. Record photocurrent densities and half-cell solar-to-hydrogen efficiencies are reported using only earth-abundant materials. Additionally, by introducing a thin TiO$_2$ passivation layer, we extend the operation to neutral electrolytes, improving environmental safety while maintaining performance. These findings establish new benchmarks for Se photocathodes and reveal the untapped potential of this simple material system for efficient, scalable, and sustainable solar hydrogen production.

[a] Micro and Nanotechnology Group, Emerging Thin Film Photovoltaics Lab, Universitat Politècnica de Catalunya (UPC), Barcelona, Spain.
  E-mail: edgardo.saucedo@upc.edu

[b] Institute of Energy Technologies and Department of Chemical Engineering, Universitat Politècnica de Catalunya (UPC), Barcelona, Spain.
  E-mail: lluis.soler.turu@upc.edu

[c] Barcelona Research Center in Multiscale Science and Engineering, Universitat Politècnica de Catalunya (UPC), Barcelona, Spain

[d] Centres Científics i Tecnològics (CCiTUB), Universitat de Barcelona, Barcelona, Spain

[e] IN2UB, Departament d'Enginyeria Electrònica i Biomèdica, Universitat de Barcelona, Barcelona, Spain

[f] School of Material Science and Engineering, Nanyang Technological University, Singapore

[g] Interdisciplinary Professional Unit in Engineering and Advanced Technologies, Instituto Politécnico Nacional, Mexico City, Mexico
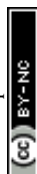
# Introduction

The growing global demand for renewable energy underscores the urgent need to develop sustainable and clean technologies that can address both environmental and energy challenges. Among these, green $H_2$ production through water splitting has emerged as a promising approach to generate clean fuel using solar energy.[1,2]

The thermodynamic potential required to split water into $H_2$ and $O_2$ is 1.23 V, involving two half-reactions: oxidation ($H_2O$ to $O_2$) and reduction ($H^+$ to $H_2$). These redox reactions can be driven by photogenerated charge carriers extracted from semiconductor materials. For efficient water splitting, the energy bands of the semiconductor must meet specific criteria: (i) the conduction band minimum (CBM) must be at a more cathodic potential than the water reduction potential ($-4.44$ eV vs. vacuum), while (ii) the valence band maximum (VBM) must be at a more anodic potential than the water oxidation potential ($-5.67$ eV vs. vacuum). This ensures that photoexcited charge carriers possess sufficient energy to drive the water-splitting reaction.[3,4] In practice, however, kinetic limitations also play an important role. Overpotentials are required to achieve appreciable reaction rates, typically on the order of 100 meV at the photocathode and 300 meV at the photoanode due to the multi-electron transfer involved in water oxidation. As a result, the minimum overall energetic requirement for photocatalytic water splitting is generally around 1.6 V.[5]

Performing both reactions on the surface of a single semiconductor can be challenging, as efficient water splitting requires charge carriers to be both energetically and physically separated. Enhancing the efficiency of the process can be achieved by spatially separating the reduction and oxidation reactions across two distinct devices. This configuration divides the required photovoltage between the two devices, reducing surface recombination losses and allowing for higher photocurrent densities and higher solar-to-hydrogen (STH) efficiency. In such systems, a photocathode is responsible for the hydrogen evolution reaction (HER), with its CBM positioned more cathodically than the water reduction potential, while a photoanode facilitates the oxygen evolution reaction (OER), with its VBM positioned more anodically than the water oxidation potential. Upon light excitation, photogenerated charge carriers are separated under the influence of selective contacts, with minority carriers migrating to the surface to drive the respective half-reaction.[6,7]

In this context, selenium (Se) has been identified as a promising photocathode material due to its favourable band alignment for HER. Se offers additional advantages, including its low toxicity, earth-abundance, and compatibility with scalable deposition techniques.[8] Despite being the first photovoltaic material discovered in 1883,[9] progress in photovoltaic (PV) power conversion efficiency has only been achieved recently, highlighting the interest in revisiting Se-based devices for optoelectronic applications. Studies on Se-based PEC devices remain limited, leaving significant potential for further exploration and optimization. To date, the highest reported photocurrent density for Se-based photocathodes is 7.2 mA cm$^{-2}$ at 0 $V_{RHE}$ (reversible hydrogen electrode), with a HC-STH efficiency of 0.39% (at 0.1 $V_{RHE}$), achieved using a FTO/Se/TiO$_2$/Pt stack in a $H_2SO_4$-based electrolyte solution.[10]

Many of the PEC systems reported in the literature rely on complex electrode architectures involving expensive materials, multilayer stacks, and/or scarce catalysts.[11] This not only increases fabrication costs but can also hinder large-scale deployment and raise concerns regarding environmental sustainability and human toxicity. In contrast, this study presents a comprehensive investigation into Se-based photocathodes, aiming to maximize performance by optimizing key parameters while maintaining simplicity, scalability, and sustainability. All materials and fabrication techniques were selected with a focus on low cost, reduced environmental impact, and minimized human health risks.

The effects of Se crystallization and film thickness are systematically examined to achieve an optimal balance between photon absorption and charge extraction. Particular attention is given to controlling the formation of specific Se phases, as these significantly influence charge transport properties and light-harvesting efficiency. In particular, trigonal selenium (t-Se) is emphasized, as it is the most common and desirable phase for PV applications due to its high carrier mobility along helical chains and favourable charge transport characteristics.[12-14] Various back contacts and electrolyte formulations are explored to improve crystal orientation and accelerate reaction kinetics. In particular, after a preliminary screening, a detailed investigation is conducted on Mo-based devices. Notably, Mo has been widely used as a back contact and substrate in chalcogenide solar cells, typically leading to high power conversion efficiencies.[15,16] In this work, this superior performance is attributed to a combination of factors, including Mo's excellent electrical conductivity, favourable band alignment, and its effect in enhancing Se crystallographic texture, all of which contribute to enhanced charge transport and reduced recombination losses. Additionally, protective layers are studied to provide surface passivation, reducing recombination losses, while still enabling efficient charge transfer. Since these overlayers act as a barrier between the semiconductor and the electrolyte, they must remain sufficiently thin (a few nanometers) to allow charge carriers to tunnel through to the electrolyte interface, where proton reduction takes place. In this way, the passivation layer both stabilizes the photocathode surface and preserves efficient catalytic activity, ultimately improving overall device performance.

Through these optimizations, this work achieves both the highest-ever efficiency and photocurrent density for a Se-based photocathode, setting a new benchmark in the field. Notably, these performances were achieved without the use of expensive nanoparticles or complex multi-layered stacks, marking a significant step toward cost-effective and scalable PEC technology. Specifically, an all-time highest HC-STH efficiency of 2.78% and a photocurrent density of 11.35 mA cm$^{-2}$ at 0 $V_{RHE}$ were obtained using soda-lime glass (SLG)/Mo/Se-based devices tested in a $H_2SO_4$-based electrolyte solution. Further advancing

the concept of sustainability and reduced toxicity, similar results (2.76% and 7.38 mA cm$^{-2}$) were achieved in a H$_2$SO$_4$-free system, with SLG/Mo/Se/TiO$_2$ devices tested in neutral phosphate buffer electrolyte, enhancing both environmental sustainability and device safety. Notably, with this modification, the higest $V_{on}$ (onset potential) reported for Se-based photocathode has been achieved as well (0.74 V$_{RHE}$).

These findings provide deeper insight into Se-based photocathodes and highlight their potential for scalable PEC applications. By improving not only performance but also material sustainability, affordability, and safety, this study aligns with ongoing efforts to develop next-generation inorganic materials for solar-driven fuel production.

# Experimental

### Device fabrication

Two substrates were utilized and analyzed: Mo-coated glass substrates (Suzhou ShangYang Solar Technology, 1 μm Mo layer) and FTO-coated glass substrates (Sigma-Aldrich, TEC 15). Before synthesizing the Se layers, the substrates underwent a sequential four-step cleaning: mechanical cleaning (with ultra-pure water and soap), ultrasonic (US) 10 min bath in isopropanol, US 10 min bath in Milli-Q water, and a 10 min Ozone cleaning.

The Se absorber layer was then deposited using a Kenosistec co-evaporation system operating at a base pressure of $5 \times 10^{-7}$ mbar. The deposition process began with the evaporation of 1 nm tellurium (Te) seed layer (Sigma-Aldrich, pellets, 99.999%), which was immediately followed by the evaporation of Se (Thermo-Scientific, 200 mesh, 99.999%) to form a layer with a thickness of 400 nm, 700 nm, or 1000 nm. Se was deposited at a controlled evaporation rate of 10–14 nm min$^{-1}$ while maintaining the substrate temperature at room temperature. The as-deposited amorphous Se (a-Se) layer was subsequently crystallized by annealing on a 200 °C hot plate for 5 min. For comparison, a-Se-based devices were also fabricated and tested.

To passivate the Se absorber, a titanium oxide (TiO$_2$) layer was deposited on the Se surface using a thermal atomic layer deposition (ALD) system (Savannah S200, Cambridge Nanotech). Tetrakis (dimethylamino)titanium(IV) (TDMAT) and deionized water (DI-H$_2$O, 16 mΩ cm) served as titanium and oxidant precursors, respectively. High-purity N$_2$ (99.999%) was used as both the purge and carrier gas. The deposition process was conducted at a chamber temperature of 120 °C and pressure of 0.3 mbar to prevent re-evaporation of Se. The pulse durations for TDMAT, DI-H$_2$O, and the purges were 0.02 s, 0.8 s, and 0.02 s, respectively. The TiO$_2$ layer thickness was precisely controlled by adjusting the number of ALD cycles. Three sample sets were prepared, targeting thicknesses of 10 nm, 25 nm, and 35 nm. To verify the deposition layer thickness, additional TiO$_2$ films were deposited onto silicon substrates and analyzed *via* ellipsometry (PLASMOS SD 2100 Ellipsometer, equipped with a 632.8 nm He–Ne laser light source).

The samples were then cut into pieces of $\sim 1$ cm$^2$. To establish electrical contact, the samples were selectively scratched to expose the underlying back contact. Indium (In) solder was used to attach a copper (Cu) wire to the exposed substrate, ensuring a reliable connection. The edges of the devices were then encapsulated using an adhesive Teflon tape to prevent any scratched areas from being exposed to the electrolyte and to the light.

### Characterization

The Se layer thickness has been measured after each deposition through X-ray fluorescence analysis (XRF, Fisherscope X-ray XDAL).

Raman measurements were performed on the surface of the samples in a backscattering configuration with a Renishaw's inVia Qontor Raman microscope using an excitation wavelength of 532 nm. The power excitation was kept at 0.5 mW. The first-order Raman spectrum of monocrystalline Si was used as a reference in all the cases.

X-ray diffraction (XRD) patterns were acquired with a Bruker D8 Advance equipment in a Bragg–Brentano configuration, using CuKα ($\lambda$ = 1.54187 Å) radiation over a $2\theta$–$\theta$ range of 20° to 80°, with a step size of 0.01°. The diffractograms have been analysed using X'Pert HighScore software. Texture coefficients (TC) have been calculated applying eqn (1), where $hkl$ are the Miller indices, $I$ is the Bragg reflection intensity from the measured pattern, $I_0$ is the Bragg reflection intensity from a reference calculated pattern (ref. 01-073-0465), and $N$ is the number of peaks considered for the analysis.[17]

$$TC_{hkl} = \frac{I_{hkl}/I_{0,hkl}}{\frac{1}{N} \cdot \sum_{i=1}^{N} I_{h_i k_i l_i}/I_{0,h_i k_i l_i}} \quad (1)$$

Scanning electron microscopy (SEM) micrographs have been obtained using a Zeiss Series Auriga Field-emission microscope, with an acceleration voltage of 5 kV, under a system vacuum of $4.17 \times 10^{-6}$ mbar, and working distances ranging between 3 to 5 mm. The samples were directly mounted on SEM stubs using conductive carbon tape.

UV-Vis-NIR spectroscopy was performed using a UV-3600 Shimadzu spectrophotometer in the 300–700 nm range with a 1 nm step size. Reflectance and transmittance data were used to calculate the absorption coefficient, and a Tauc plot of $[\alpha h\nu]^2$ *vs.* $E$(eV) was constructed to estimate the optical band gap energies of the synthesized Se-based photocathodes by extrapolating the linear region and using a modified version of the Tauc's equation as elsewhere reported.[18]

The X-ray photoelectron spectroscopy (XPS) analysis was carried out in ESFOSCAN at the CCiTUB, an equipment based on the PHI VersaProbe 4 instrument from Physical Electronics (ULVAC-PHI). Measurements have been done with a monochromatic focused X-ray source (Aluminium Kalfa line of 1486.6 eV) calibrated using the 3d5/2 line of Ag with a full width at half maximum (FWHM) of 0.6 eV. The area analyzed was a circle of 100 microns in diameter, and the resolution selected for the

spectra was 224 eV of pass energy and 0.8 eV per step for the general spectra and 27 eV of pass energy and 0.1 eV per step for high-resolution spectra of the selected elements. The analysis and fitting of the spectra were made with Multipak V. 9.9.2 program. All measurements were performed in an ultra-high vacuum (UHV) chamber at a pressure between $5 \times 10^{-10}$ and $5 \times 10^{-9}$ Torr.

The PEC performances were evaluated using an Autolab workstation in a standard three-electrode configuration (Fig. 1(a)) at room temperature. The Se-based device functioned as the working electrode (WE), while platinum foil served as the counter electrode (CE) (Metrohm, 1 cm$^2$ effective area). An Ag/AgCl electrode in 3 M KCl acted as the reference electrode (RE) (Metrohm). Two distinct electrolyte solutions were tested: 0.5 M H$_2$SO$_4$ solution (SA); 1 M phosphate-buffered solution (PB), comprising monobasic dihydrogen phosphate (KH$_2$PO$_4$) and dibasic monohydrogen phosphate (K$_2$HPO$_4$) mixed in a 1:2 ratio. Each device has been tested with a freshly prepared electrolyte solution, which underwent a 20 min purge under controlled N$_2$ continuous flux to ensure a proper current (j) correlation to hydrogen evolution on the surface of each tested photocathode.

Simulated sunlight was provided using a calibrated AAA Ossila solar simulator equipped with an LED lamp, operating under 1 Sun AM 1.5 conditions. A consistent working distance of 8.5 cm was maintained between the lamp and the WE. Irradiance was confirmed using a Thorlabs digital handheld optical power and energy meter console, paired with an integrating sphere for enhanced precision. To ensure uniform and accurate illumination, the active area of each WE was restricted to ~1 cm$^2$. The precise effective area of each device was digitally computed to ensure accurate current density ($J$) calculations. Based on the Autolab workstation sensitivity (10 nA) and digital area resolution (0.01 mm) accuracy, $J$ values are reported with two decimal places, disregarding experimental biases in the Autolab measurements.

Linear sweep voltammetry (LSV) was performed using a cathodic scan direction at a scan rate of 0.01 V s$^{-1}$. Chopped light measurements were performed using a custom-designed external mechanical shutter, which operated on a 4-second cycle (2 seconds illumination, 2 seconds dark).

Elemental analysis of the electrolyte solutions after LSV measurements was carried out using inductively coupled plasma optical emission spectroscopy (ICP-OES, Agilent Technologies, 5100).

Chronoamperometry was performed under chopped light illumination, by applying a fixed voltage corresponding to the maximum efficiency point, determined from the HC-STH analysis of each device.

Photoelectrochemical impedance spectroscopy (PEIS) measurements were obtained considering a frequency range from 100 kHz to 100 Hz at 0 V$_{RHE}$. The resulting impedance spectra were fitted using an equivalent circuit model with ZView software.

Voltage open circuit potential ($V_{ocp}$) measurements were performed under illumination for 1 min till stabilization, followed by 9 min under dark conditions.

H$_2$ detection was carried out using a calibrated micro gas chromatograph (Micro-GC 490 PRO), connected in-line with a mass flow controller that injected N$_2$ at 20 mL min$^{-1}$ into a sealed cell, enabling comprehensive analysis of the photoelectrochemical reaction products.
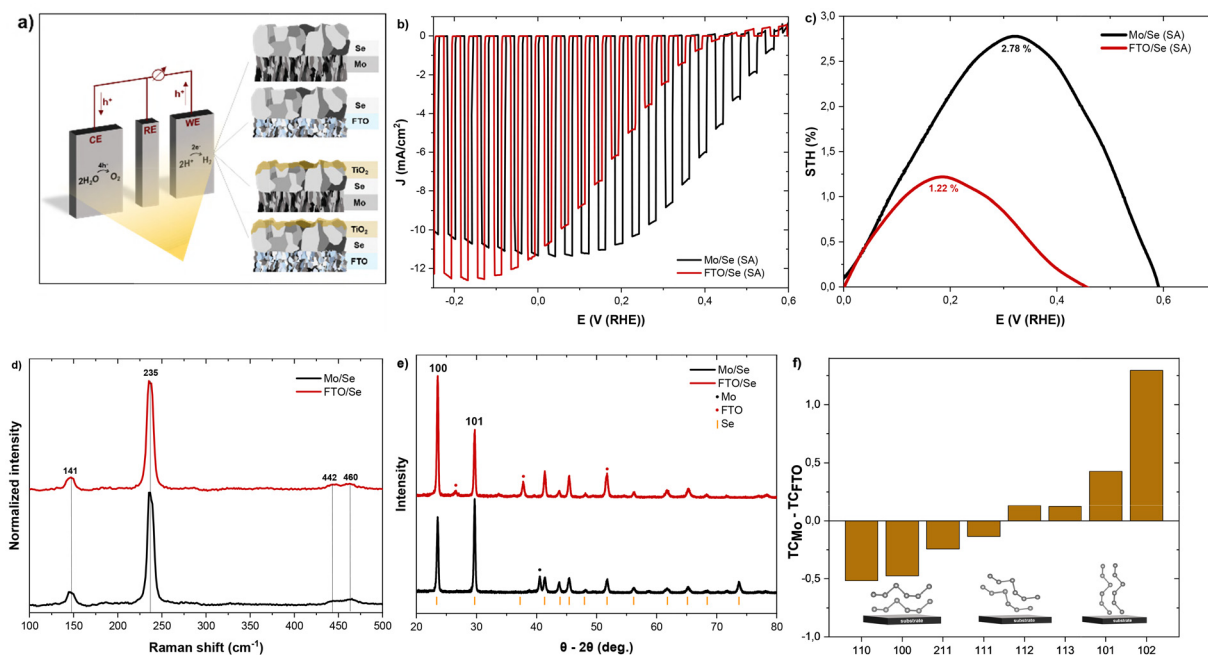


Fig. 1 PEC set up and main stacks tested (a). Photocurrent density under chopped light (b) and corresponding half-cell STH efficiency (c). Raman spectra (d), XRD patterns (e) and texture coefficient difference (f) of Se grown on Mo and FTO.

To systematically compare the various devices and solutions, the applied potential *versus* the Ag/AgCl reference electrode ($V_{Ag/AgCl}$) was converted to the reversible hydrogen electrode ($V_{RHE}$) scale using the Nernst equation (eqn (2)):[19]

$$V_{RHE} = V_{Ag/AgCl} + E^0_{Ag/AgCl} + \frac{R \cdot T \cdot \ln(10) \cdot pH}{F} \qquad (2)$$

where $V_{Ag/AgCl}$ is the applied potential at the Ag/AgCl reference electrode, $E^0_{Ag/AgCl}$ is the standard potential of the Ag/AgCl reference electrode (0.197 V), pH is the pH of the electrolyte (7 for PB and 0.3 for SA), $R$ is the universal gas constant (8.314 J mol$^{-1}$ K$^{-1}$), T is the temperature (298 K), $F$ is Faraday's constant (96 485 C mol$^{-1}$). The HC-STH efficiency was determined using eqn (3):[20]

$$HC\text{-}STH = \frac{J \times (V_{RHE} - V_{H^+/H_2})}{P_{sun}} \times 100\% \qquad (3)$$

where $J$ is the photocurrent density (mA cm$^{-2}$), $V_{H^+/H_2}$ is the hydrogen reduction potential (0 V$_{RHE}$), $P_{sun}$ is the simulated solar intensity under AM 1.5G conditions (100 mW cm$^{-2}$). The reported HC-STH values and their associated confidence intervals have been calculated from the average $J$ value of three repetitions of each experiment to ensure the accuracy of the reported values.

## Results and discussion

The influence of the absorber's crystallographic, structural and morphological properties on PEC performance was systematically investigated. A broad screening of device architectures was carried out, varying the back contact (Mo and FTO), absorber thickness (400 nm, 700 nm, and 1000 nm), and Se phase (amorphous and crystalline). The two boundary thicknesses were selected based on previous benchmarks: 400 nm corresponds to the highest reported PEC efficiency for Se-based photocathodes,[10] while 1000 nm matches the absorber thickness used in the most efficient Se-based solar cells to date.[8] All devices were characterized *via* LSV in SA to evaluate their photoresponse, identify possible parasitic reactions beyond HER, and extract key performance metrics including $J$, $V_{on}$, and HC-STH efficiency. A summary of the main LSV curves is presented in Fig. S1. For a-Se, 400 nm thick absorbers exhibited a measurable photo-response, whereas the 1000 nm layers did not, regardless of the back contact (Mo or FTO). This lack of response is attributed to the high resistivity of a-Se, which limits charge transport.[21] When comparing samples with the same Se thickness but different phases, crystallized Se consistently outperformed a-Se across all tested conditions. Furthermore, within the crystallized Se samples, the 1000 nm thick absorbers demonstrated superior performance compared to their 400 nm counterparts, independent of the substrate. This improvement is likely due to the increased light absorption[10] and lower resistivity of crystallized Se, which enhances charge generation and transport. Devices with 700 nm crystalline Se showed intermediate behavior, bridging the performance gap between the thinner and thicker absorbers. For this reason, from this point onward, all subsequent discussions will focus exclusively on 1000 nm crystallized Se-based architectures. A schematic summary of the main stacks tested is presented in Fig. 1(a).

Reflectance and transmittance measurements were used to calculate the absorption coefficient ($\alpha$), and a Tauc analysis was performed to estimate the optical band gap of the Se absorber (Fig. S2). The extrapolation of the linear region in the $[\alpha h\nu]^2$ *vs.* $h\nu$ plot indicates a direct allowed band gap of 1.9 eV. This value is consistent with previously reported optical gaps for t-Se, confirming that the material exhibits the expected direct transition. Based on this band gap, the theoretical maximum $J$ under AM 1.5 illumination can be estimated to be ∼16.2 mA cm$^{-2}$.[22] To further validate the reliability of the band gap determination, the Tauc plot includes data extending to higher photon energies, ensuring that the extrapolation was performed from a clearly linear region and minimizing uncertainty in the band edge assignment.

Fig. 1 presents the $J$ (b) and HC-STH efficiency (c) under simulated AM 1.5 irradiation for the best-performing devices tested in SA-based electrolyte solutions. At 0 V$_{RHE}$, both Mo/Se and FTO/Se achieved a $J$ of 11.35 mA cm$^{-2}$, setting a new benchmark for Se-based photocathodes. Evaluating the HC-STH efficiency, values of 2.78% and 1.22% were recorded for Mo and FTO, respectively, both exceeding the previous state-of-the-art. Compared to the previously reported best-performing bare Se photocathode (1.4 mA cm$^{-2}$, 0.05%),[10] the Mo/Se configuration exhibits over 8× higher $J$ and more than 55× higher HC-STH efficiency. When benchmarked against the best-performing Se-based full-stack architecture incorporating TiO$_2$ and Pt (7.2 mA cm$^{-2}$, 0.39%),[10] the simplified Mo/Se system still outperforms by approximately 1.6× in $J$ and 7× in HC-STH efficiency, demonstrating the cost-effectiveness and competitiveness of the approach. In addition, LSV reveals a more positive $V_{on}$ for Mo/Se (0.56 V$_{RHE}$) compared to FTO/Se (0.45 V$_{RHE}$), indicating improved photovoltage generation and more efficient charge extraction. In both cases, the present devices outperform the previous benchmark $V_{on}$ values (0.4 V$_{RHE}$).

The higher efficiency observed with Mo-based devices can be attributed to a combination of factors that boost HER. To verify the phase purity and crystallinity of the Se absorber layers, Raman spectroscopy was performed on both Mo/Se and FTO/Se photocathodes (Fig. 1(d)). The spectra show the characteristic peaks of t-Se,[23,24] with no evidence of additional phases or secondary compounds. This confirms that both absorbers are constituted of pure t-Se, thereby excluding differences in crystalline phase as a factor behind the observed variations in PEC.

In terms of morphology, SEM images reveal that the growth behaviour of Se is independent of the underlying substrate, displaying similar structural characteristics on both Mo (Fig. 2(b)) and FTO substrates (Fig. S3). In both cases, the Se films exhibit a characteristic double-layer grain structure, consisting of a compact base layer of smaller grains (∼200 nm) and an overlying layer of larger (∼1 µm), more laterally extended grains. This morphology ensures complete coverage
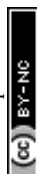
of the substrate, reducing the probability of direct recombination between photogenerated $e^-$ at the Se surface and $h^+$ collected at the back contact. Additionally, the dual-layer grain structure increases the effective surface area, which is particularly advantageous for the HER, a surface-driven process.

The improved activity of Mo/Se over FTO/Se could then be attributed to other factors, including Mo's higher reflectivity, which enhances photon absorption by reflecting incident light into the absorber, increasing the overall light absorption in the Se layer. Secondly, it can be related to variations in the crystallographic texture of Se layers induced by the underlying substrate. This interpretation is first supported by direct inspection of the XRD patterns of both samples (Fig. 1(e)). Both Mo/Se and FTO/Se exhibit sharp, well-defined peaks consistent with crystalline t-Se, with hexagonal structure and space group $P3_121$, $Z = 3$ (Fig. S4). However, variations in peak intensity suggest distinct substrate-driven growth behaviour. For instance, the most intense Bragg reflection observed in the FTO/Se sample corresponds to the (100) crystallographic plane, indicating a preferential orientation along crystallographic directions parallel to the substrate surface; *i.e.*, within the [h00] zone axis. Otherwise, the absence of (00*l*) reflections suggests a minimal contribution from crystallites oriented with their *c*-axis perpendicular to the substrate. In contrast, the Mo/Se sample exhibits its strongest diffraction peak at the (101) plane, indicative of a higher prevalence of crystallites with tilted orientations with respect to the substrate's surface, hence reflecting a greater *c*-axis contribution. These results demonstrate that the choice of substrate has a direct impact on the crystallographic characteristics of the deposited Se layer. Specifically, the Mo substrate appears to promote Se crystallization along orientations that expose edge-rich, catalytically active facets, which may contribute to the observed PEC-enhanced performance.[25]

This trend is further confirmed by the texture coefficient (TC) analysis shown in Fig. S5. The TC plot reveals that crystallographic planes which crystallographic orientation is parallel to the substrate's surface, such as (110) and (100), are more dominant when using FTO, while orientations with a higher inclination angle (*i.e.* more vertically-oriented), including (101) and (102), are prevalent on Mo substrate. The difference in texture coefficients for each plane between the two substrates is shown in the $\Delta TC = TC_{Mo} - TC_{FTO}$ plot (Fig. 1(f)), which further emphasizes this divergence, exhibiting a systematic increase in the TC disparity between Mo and FTO-grown films. In this plot, $\Delta TC_{hkl} = 0$ indicates that the (*hkl*) family of planes is equally represented regardless of the substrate. On the other hand, it can be confirmed that planes corresponding to mostly horizontal texture (*hk*0 planes, where $h + k$ is highest) are prevalent in FTO/Se films ($\Delta TC < 0$). In contrast, Mo/Se layers exhibit an enhanced preference for vertically oriented growth, characterized by (hkl) planes with the highest $k + l$ contributions, as described in previous studies.[26] This observation ($\Delta TC > 0$) suggests that the Mo substrate facilitates the preferential formation of vertically aligned Se ribbons, which favours the catalytic activity.

To confirm that the photocurrent of the champion device originates from $H_2$ generation, GC analysis were performed during PEC operation, and a distinct $H_2$ signal was directly detected (Fig. S6). This result verifies that the measured current corresponds to $H_2$ evolution rather than parasitic side reactions. To further rule out possible photocorrosion contributions, a full set of post-characterization analyses is presented later in the manuscript, including XPS, Raman, XRD, and ICP-OES. Together, these complementary measurements demonstrate that the device maintains its structural and chemical integrity under operation, providing confidence that the photocurrent is dominated by the hydrogen evolution reaction.

To advance the sustainability and safety of the PEC system, and focusing on the top-performing devices in terms of efficiency (Mo/Se) a second optimization step was performed, replacing SA with PB electrolyte solution. This substitution aimed to enhance environmental compatibility and reduce toxicity while maintaining high performance. $H_2SO_4$ is highly corrosive and hazardous, posing significant handling risks, including severe burns, respiratory hazards, and equipment degradation. Moreover, its disposal requires strict environmental controls to prevent acidification and contamination.[27] In contrast, neutral phosphate buffer can be considered to be less toxic and more biocompatible, making it a safer and more scalable alternative for PEC applications.

Devices were fabricated and tested under identical conditions to the ones presented above, with only the electrolyte solution being changed. As expected in terms of *J*, a slight reduction was observed, specifically, *J* decreased from 11.35 mA cm$^{-2}$ (Mo/Se in SA, Fig. 1(b)) to 8.90 mA cm$^{-2}$ (Mo/Se in PB, Fig. 2(c)). Considering HC-STH efficiency, a reduction from 2.78% (Mo/Se in SA, Fig. 1(c)) to 2.13% (Mo/Se in PB, Fig. 2(d)) was detected. The electrolyte significantly influences reaction kinetics and charge transfer at the semiconductor/ electrolyte interface. Since HER is a proton reduction reaction, and since fewer protons ($H^+$) are available in PB rather than in SA, this change of electrolyte results in a slower reduction half reaction ($2H^+ + 2e^- \rightarrow H_2$), leading to lower *J* and HC-STH.

To prevent performance losses in PB, an additional $TiO_2$ layer was deposited on top of the Se absorber. This modification was intended to enhance charge transfer and passivate surface states, ultimately boosting the HC-STH efficiency.[28,29] Multiple sets of devices were synthesized, incorporating $TiO_2$ layers with target thicknesses of 10 nm, 25 nm, and 35 nm, deposited by ALD. Ellipsometry measurements performed on Si substrates simultaneously coated with $TiO_2$ confirmed actual thicknesses of 109 Å, 247 Å, and 324 Å, respectively.

SEM cross-section presented in Fig. 2(a) reveals the full architecture of the Mo/Se/$TiO_2$ photocathode. The Se absorber layer is formed by large, well-defined grains, which are beneficial for facilitating directed charge transport across the film and minimizing grain boundary recombination. The large grain size also implies a reduced density of horizontal grain boundaries, which can otherwise act as charge-trapping sites and hinder vertical carrier transport. Finally, a thin conformal $TiO_2$ layer is evident on top of the Se, providing surface
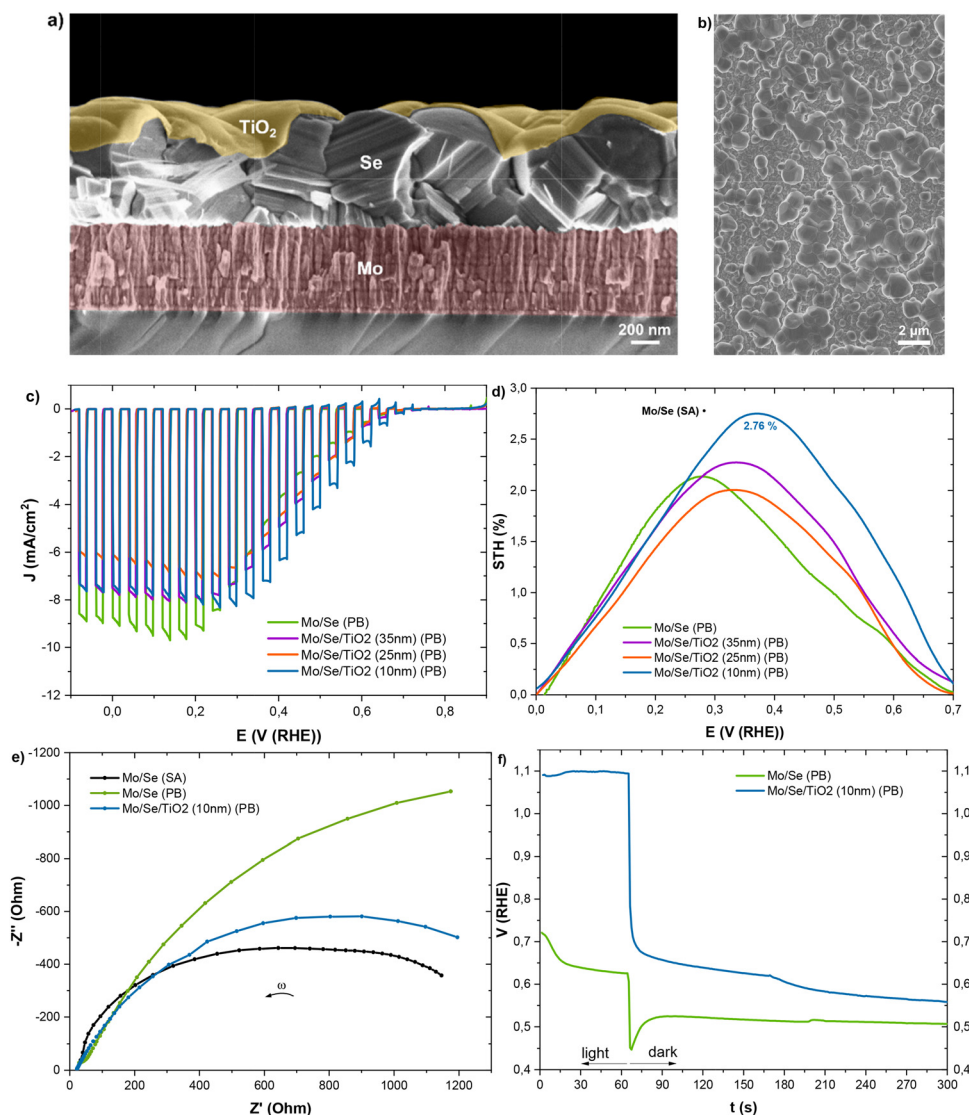
**Fig. 2** Cross-sectional SEM image of Mo/Se/TiO$_2$ (a). Top-view SEM image of Mo/Se (b). $J$ under chopped illumination (c) and corresponding HC–STH efficiency (d). Nyquist plots (e). $V_{ocp}$ measurements (f).

passivation while preserving the underlying microstructure. The sharp interfaces between layers, the absence of voids or cracks, and the favourable morphology of Se collectively contribute to the efficient charge separation and transport observed in device performance.

Comparing the LSV voltammetry curves (Fig. 2(c)) and corresponding HC-STH (Fig. 2(d)) of the Mo/Se/TiO$_2$ devices tested in PB, the 10 nm TiO$_2$ layer was found to be the optimal thickness, leading to HC-STH gains. Notably, the HC-STH efficiency went from 2.13% for the bare absorber to 2.76% after the deposition of 10 nm TiO$_2$, fully recovering the performance lost by switching from SA to PB. In terms of $V_{on}$, all the devices tested showed an improvement compared to SA, presenting a more positive $V_{on}$ (0.74 $V_{RHE}$), the highest reported for Se-based photocathodes.

To gain deeper insight into the impact of TiO$_2$ passivation on the PEC response, charge carrier dynamics were evaluated

under light for three systems: Mo/Se in SA, Mo/Se in PB, and Mo/Se/TiO$_2$ (10 nm) in PB. Fig. 2(e) shows the corresponding Nyquist plots for the three photocathodes. The results reveal that when switching from SA to PB electrolyte, the semicircle radius of the bare Mo/Se photocathode increases significantly, indicating a rise in charge transfer resistance and hence slower interfacial charge transfer kinetics.[30] This result confirms that the neutral pH environment of PB hinders PEC performance compared to the more acidic SA electrolyte. However, upon introducing a 10 nm TiO$_2$ layer on top of Se and testing the device in PB, the semicircle radius markedly decreases, nearly matching the value observed for Mo/Se in SA. To quantify these trends, the Nyquist plots were fitted using an equivalent circuit model (Z view).[31] The extracted charge transfer resistance values were 1471 Ω for Mo/Se in SA, 2758 Ω for Mo/Se in PB, and 1633 Ω for Mo/Se/TiO$_2$ in PB. This indicates that TiO$_2$ passivation effectively mitigates the kinetic limitations

imposed by the PB environment, enhancing interfacial charge transfer and reducing recombination losses. This finding further supports the use of thin $TiO_2$ layers as a sustainable strategy to boost performance without resorting to harsher or less environmentally friendly electrolytes.

$V_{ocp}$ analysis was conducted under light and dark conditions in PB (Fig. 2(f)). Upon illumination, both Mo/Se and Mo/Se/$TiO_2$ electrodes show a clear positive shift in potential, indicating effective photoinduced charge separation even without an external bias. However, the Mo/Se/$TiO_2$ electrode achieves a significantly higher photovoltage (1.09 $V_{RHE}$) compared to bare Mo/Se (0.63 $V_{RHE}$), demonstrating enhanced interfacial quality and more efficient charge separation. Notably, the $TiO_2$-modified sample also maintains a higher potential in the dark, suggesting improved surface passivation and suppression of non-radiative charge loss pathways. As a result, the $TiO_2$ layer compensates for the performance drop typically observed in neutral electrolytes, enabling photocurrent levels comparable to those of unmodified Se tested in acidic conditions. Further insight into interfacial dynamics can be drawn from the transient response after light-off. In the Mo/Se electrode, a sharp dip in $V_{ocp}$ is followed by slow recovery, linked to fast recombination and delayed charge redistribution. In contrast, the Mo/Se/$TiO_2$ sample exhibits a much smoother decay profile, consistent with reduced defect activity. These findings highlight the dual role of $TiO_2$ as both a protective and electronic interfacial layer, enabling higher photovoltage and better stability under mild operating conditions.

For comparison, the same methodology was applied to devices grown on FTO substrates. Consistently, Mo-based photocathodes outperformed all FTO-based counterparts in terms of efficiency, in both SA and PB. Similar to the Mo-based devices, an optimal $TiO_2$ thickness of 10 nm was also identified for FTO samples, yielding a maximum HC-STH efficiency of 1.66% in PB, representing the highest performance recorded for FTO-based devices. A summary of the HC-STH efficiency obtained is provided in Fig. 3. Notably, all the optimized devices demonstrated improved performance compared to the previously reported benchmarks. The corresponding LSV curves and HC-STH plots for each configuration are provided in Fig. S7.

To assess the stability of the champion Se-based photocathodes during PEC measurements, complementary analyses were carried out on both the used devices and the corresponding electrolytes. These tests were designed to ensure that the PEC responses reported here reflect intrinsic device performance rather than photocorrosion or parasitic reactions.

Electrolyte samples were analyzed by ICP-OES to detect possible leaching of device components during operation. Two cases were examined: SA after LSV on SLG/Mo/Se and PB after LSV on SLG/Mo/Se/$TiO_2$ (10 nm). In both cases, the concentrations of Se and Ti remained below the detection limits ($<100$ ppb for Se and $<53$ ppb for Ti) (Table S8), indicating no dissolution of the photoabsorber and protection layer under the applied PEC conditions.

Raman spectroscopy performed on SLG/Mo/Se after LSV in SA revealed the same characteristic peaks of t-Se as in fresh samples, confirming that the crystallinity of the absorber is preserved during PEC operation. This conclusion is further supported by XRD analysis (Fig. S9), which shows that the diffraction pattern of the sample after PEC testing is identical to that of the fresh sample. Both sets of measurements demonstrate that the Se layer retains its crystalline phase after electrochemical operation, indicating that the structural integrity of the photocathodes is maintained during the PEC experiments.

XPS analysis (Fig. S10) was performed on SLG/Mo/Se before and after LSV testing in SA electrolyte to further evaluate the chemical stability of the photocathodes. The survey spectra confirms that the overall elemental composition is preserved, with Se and features unchanged. The high-resolution Se 3d spectra show nearly identical peak positions and shapes for both fresh and used samples, confirming that Se remains in its elemental state after PEC operation and that no Se oxides are formed. The C 1s region is dominated by the C–H peak at $\sim 284.8$ eV and shows no significant change after LSV, consistent with typical surface adventitious carbon. The main difference observed is in the O 1s region, where a peak at $\sim 532.5$ eV appears in the samples after LSV. This binding energy is associated with O–H species, most likely originating from adsorbed water or hydroxyl groups from the acidic electrolyte,
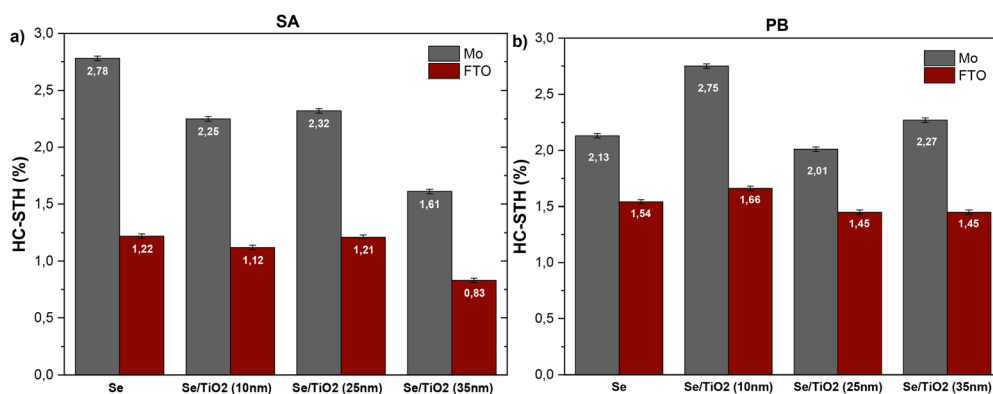


**Fig. 3** HC-STH efficiency of Mo-based and FTO-based Se photocathodes tested in SA (a) and PB (b).

rather than Se oxides, which would appear at lower binding energies ($\sim$530–531 eV).[32]

Finally, chronoamperometry was conducted on SLG/Mo/Se (in SA) at a fixed voltage corresponding to the maximum efficiency point extracted from the HC-STH analysis. The photocurrent stabilized rapidly and remained constant throughout the measurement (Fig. S11). Since the longest PEC experiments reported here are LSV scans ($\sim$90 s), while chronoamperometry demonstrated stable operation for over 140 s, these results confirm that the photocathodes remain stable over the entire duration of the PEC measurements presented in this work. These results corroborate the ICP-OES, Raman, XRD and XPS analyses, supporting that the Mo/Se photocathodes remain chemically stable under the applied PEC conditions and that the observed PEC activity is not driven by photocorrosion.

Table 1 summarizes key PEC performance metrics of the champion devices developed in this work compared to previously reported chalcogenide-based photocathodes. Most referenced systems rely on complex device stacks, typically involving multilayer architectures based on multi-element absorbers such as $Cu_2ZnSn(S,Se)_4$, $Cu_2ZnSnSe_4$, and $Cu(In,Ga)Se_2$. In contrast, the photocathodes reported in the present study are based on a simple, single-element absorber. Moreover, unlike this work, the use of Pt as a catalyst is widespread among previous studies to boost device performance, further increasing system cost and complexity. Regarding the electrolyte, most high-efficiency systems operate exclusively under strongly acidic conditions (highlighted in red), while this work demonstrates comparable high performance even under neutral conditions (highlighted in blue), enhancing environmental safety and operational stability. In terms of photoelectrochemical performance, the Mo/Se photocathode achieves an HC-STH efficiency of 2.78% and a $J$ of 11.35 mA cm$^{-2}$ at 0 $V_{RHE}$, surpassing all previously reported Se-based systems and performing comparably to or better than much more complex multi-element devices. Additionally, the $V_{on}$ of 0.74 $V_{RHE}$ for Mo/Se tested in PB is among the most positive reported, indicating effective photovoltage generation and efficient charge extraction.

Fig. 4 shows the band edge positions of several chalcogenide absorbers elsewhere reported, which have been plotted relative to the normal hydrogen electrode (NHE) scale. The CBM and VBM of each material are compared to the water splitting redox potentials. Among the materials presented, Se exhibits a conduction band that is well above the HER threshold, ensuring a strong driving force for H$^+$ reduction. Simultaneously, Se maintains a sufficiently deep valence band that minimizes the risk of oxidative photo-corrosion, unlike some materials such as CZTSSe, which have VBM positions closer to the OER threshold and may suffer multiple issues when no additional layers are applied. This favourable band alignment, together with its low toxicity and processing simplicity, further supports the potential of Se as a highly effective and sustainable photocathode material for solar hydrogen production. Altogether, this comparison highlights how the minimalist, low-cost, and nanoparticle-free strategy developed in this work enables high PEC performance without sacrificing simplicity, scalability, or sustainability.

## Conclusion

This work demonstrates that high-efficiency PEC green H$_2$ production can be achieved using simple, low-cost, and environmentally conscious Se-based photocathodes. Through a comprehensive screening of Se thickness, phase, back contact, protective overlayers, and electrolyte composition, we identified a device configuration (Mo/Se) that delivers a HC-STH efficiency of 2.78 $\pm$ 0.01% and a photocurrent density of 11.35 $\pm$ 0.01 mA cm$^{-2}$ at 0 $V_{RHE}$ in acidic electrolyte, setting a new performance benchmark for Se in PEC applications. Moreover, a comparable performance (2.76 $\pm$ 0.01%, 7.38 $\pm$ 0.01 mA cm$^{-2}$) was achieved under neutral conditions by introducing a 10 nm TiO$_2$ layer, eliminating the need for hazardous media and obtaining the highest $V_{on}$ reported so far (0.74 $V_{RHE}$). A Se thickness of 1000 nm was found to be optimal, balancing light absorption with efficient charge extraction. Additionally, Mo consistently outperformed FTO as a back contact across all tested conditions, offering improved photovoltage, charge transfer, and enhanced crystallographic texture. These results were obtained without the use of expensive catalysts, noble metals, or complex

**Table 1** Recently reported photocathodes and relative PEC metrics

| Device stack | $E_g$ (eV) | Electrolyte | HC-STH (%) | $V_{on}$ ($V_{RHE}$) | $J$ (mA cm$^{-2}$) | Ref. |
|---|---|---|---|---|---|---|
| Mo/Se | 1.86 | 0.5 M H$_2$SO$_4$ | 2.78 | 0.56 | −11.4 | This work |
| Mo/Se/TiO$_2$ | 1.86 | 1 M PB | 2.76 | 0.74 | −7.4 | This work |
| FTO/Se | 1.86 | 0.5 M H$_2$SO$_4$ | 1.22 | 0.45 | −11.4 | This work |
| FTO/Se | 1.94 | 0.5 M H$_2$SO$_4$ | 0.05 | 0.40 | −1.4 | 10 |
| FTO/Se/TiO$_2$/Pt | 1.94 | 0.5 M H$_2$SO$_4$ | 0.39 | 0.41 | −7.2 | 10 |
| FTO/Sb$_2$S$_3$/TiO$_2$/Pt | 1.20 | 1.0 M H$_2$SO$_4$ | — | 0.25 | −3.4 | 33 |
| FTO/Sb$_2$S$_3$/CdS/TiO$_2$/Pt | 1.70 | 0.5 M Na$_2$SO$_4$ | 0.64 | 0.50 | −6.0 | 34 |
| FTO/Sb$_2$Se$_3$/CdS/TiO$_2$/Pt | 1.23 | NaPi buffer | 0.68 | 0.43 | −8.6 | 28 |
| Mo/Cu$_2$ZnSn(S,Se)$_4$/CdS/TiO$_2$/Pt | 1.10 | 0.5 M H$_2$SO$_4$ | 6.47 | 0.50 | −40.4 | 35 |
| Mo/Cu$_2$ZnSnS$_4$/HfO$_2$/CdS/HfO$_2$/Pt | 1.50 | 0.2 M NaH$_2$PO$_4$ | 7.27 | 0.72 | −28.0 | 36 |
| Mo/Cu$_2$ZnSnS$_4$/CdS/TiO$_2$/Pt | 1.50 | 0.5 M H$_2$SO$_4$ | 9.91 | 0.73 | −29.4 | 37 |
| Mo/Cu$_2$ZnSnSe$_4$/CdS/ZnO/ITO/MoS$_2$ | 1.05 | 1 M PB | — | 0.43 | −18.0 | 38 |
| Mo/Cu$_2$ZnSnSe$_4$/CdS/TCO/TiO$_2$/Pt | 1.05 | 0.5 M H$_2$SO$_4$ | 7.00 | 0.45 | −37.0 | 39 |
| Mo/Cu(In,Ga)Se$_2$/CdS/Al$_2$O$_3$/TiO$_2$/Pt | 1.10 | 1.0 M HClO$_4$ | 9.30 | 0.63 | −28.0 | 40 |
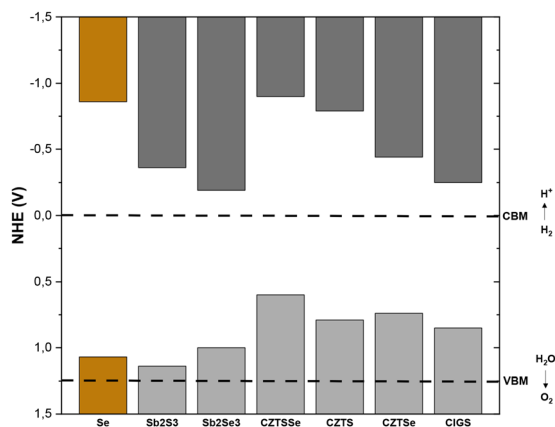
**Fig. 4** Band edge positions[28,33,35,37,38,40] of commonly studied photo-cathode materials relative to NHE, along with the redox potentials required for water splitting.

multilayer stacks, relying exclusively on earth-abundant, low-toxicity materials and scalable fabrication methods. Altogether, this study redefines the potential of Se in solar fuel technologies and establishes a clear pathway toward scalable, sustainable, and high-performing PEC architectures. This work demonstrates that simplicity and performance are not mutually exclusive, and that impactful solar $H_2$ production might be achieved without overengineering.

## Author contributions

Edoardo Maggi: writing, original draft, methodology, investigation, formal analysis, conceptualization. Oriol Segura Blanch: methodology, investigation, review. Arnau Torrens: methodology, investigation, review. Ivan Caño: methodology, investigation, writing, review. Alex Jimenez-Arguijo: investigation, writing, review. Pau Estarlich: methodology, investigation. Lorenzo Calvo-Barrio: methodology, investigation. Mario F. Garcia-Sanchez: review. Hao Zhe Chun: methodology. Marcel Placidi: review. Joaquim Puigdollers: review. Jordi Llorca: review. Lydia Helena Wong: review. Lluis Soler: writing, review and editing, methodology, conceptualization, validation, resources, funding acquisition, supervision. Edgardo Saucedo: writing, review and editing, methodology, conceptualization, validation, resources, funding acquisition, supervision.

## Conflicts of interest

There are no conflicts of interest to declare.

## Data availability

All data supporting the findings of this study, including characterization datasets from Raman spectroscopy, X-ray diffraction, UV-Vis-NIR spectroscopy, linear sweep voltammetry, open-circuit voltage measurements, and photoelectrochemical

impedance spectroscopy, are available in the Zenodo repository at **https://doi.org/10.5281/zenodo.15553906**.

The supplementary information provides additional experimental data, including optical, structural, and electrochemical characterizations of Se-based photocathodes. It features LSV, GC, and chronoamperometry analyses, as well as Raman, XRD, XPS, and ICP-OES results before and after PEC testing. These data confirm device performance, stability, and the chemical integrity of the Se absorber. See DOI: **https://doi.org/10.1039/d5ey00297d**.

## Acknowledgements

## References

1 J. H. Kim, D. Hansora, P. Sharma, J.-W. Jang and J. S. Lee, Toward Practical Solar Hydrogen Production – an Artificial Photosynthetic Leaf-to-Farm Challenge, *Chem. Soc. Rev.*, 2019, **48**(7), 1908–1971, DOI: **10.1039/C8CS00699G**.

2 Y. Bicer and I. Dincer, Assessment of a Sustainable Electrochemical Ammonia Production System Using Photoelectrochemically Produced Hydrogen under Concentrated Sunlight, *ACS Sustainable Chem. Eng.*, 2017, **5**(9), 8035–8043, DOI: **10.1021/acssuschemeng.7b01638**.

3 H. Idriss; M. Scott and V. Subramani, Introduction to Hydrogen and Its Properties, *Compendium of Hydrogen Energy*, Elsevier, 2015, pp. 3–19, DOI: **10.1016/B978-1-78242-361-4.00001-7**.

4 S. Nishioka, F. E. Osterloh, X. Wang, T. E. Mallouk and K. Maeda, Photocatalytic Water Splitting, *Nat. Rev. Methods Primers*, 2023, **3**(1), 42, DOI: **10.1038/s43586-023-00226-x**.

5 A. A. Mamun, A. Billah and M. Anisuzzaman Talukder, Effects of Activation Overpotential in Photoelectrochemical Cells Considering Electrical and Optical Configurations, *Heliyon*, 2023, **9**(6), e17191, DOI: **10.1016/j.heliyon.2023.e17191**.

6 G. G. Bessegato, T. T. Guaraldo, J. F. de Brito, M. F. Brugnera and M. V. B. Zanoni, Achievements and Trends in Photoelectrocatalysis: From Environmental to Energy Applications, *Electrocatalysis*, 2015, **6**(5), 415–441, DOI: **10.1007/s12678-015-0259-9**.

7 N. Pirrone, F. Bella and S. Hernández, Solar H2 Production Systems: Current Status and Prospective Applications, *Green Chem.*, 2022, **24**(14), 5379–5402, DOI: **10.1039/D2GC00292B**.

8 Q. Liu, X. Wang, Z. Li, W. Lu, X. Wen, X. An, M. Feng, H. Yan, J. Hu and D. Xue, Standing 1D Chains Enable Efficient Wide-Bandgap Selenium Solar Cells, *Adv. Mater.*, 2025, **37**(1), 2410835, DOI: **10.1002/adma.202410835**.

9 C. E. Fritts, On a New Form of Selenium Cell, and Some Electrical Discoveries Made by Its Use, *Am. J. Sci.*, 1883, **s3–26**(156), 465–472, DOI: **10.2475/ajs.s3-26.156.465**.

10 J. Li, D. Li, F. Gao, Y. Han, J. Yan and S. Liu, Enabling Solar Hydrogen Production over Selenium: Surface State Passivation and Cocatalyst Decoration, *ACS Sustainable Chem. Eng.*, 2021, **9**(29), 9923–9931, DOI: **10.1021/acssuschemeng.1c03066**.

11 M. Kumar, B. Meena, P. Subramanyam, D. Suryakala and C. Subrahmanyam, Recent Trends in Photoelectrochemical Water Splitting: The Role of Cocatalysts, *NPG Asia Mater.*, 2022, **14**(1), 88, DOI: **10.1038/s41427-022-00436-x**.

12 C. Guarneros-Aguilar, O. Calzadilla, J. A. Barón-Miranda, J. L. Fernandez-Muñoz and F. Caballero-Briones, Phase Control in Selenium Electrodeposition with Bath Temperature and Deposition Potential, *Mater. Res. Express*, 2019, **6**(6), 066412, DOI: **10.1088/2053-1591/ab0875**.

13 X. Liu, W. Zhang, Q. Li, J. Wang, E. Liu, H. Miao and X. Hu, In-Situ Construction of S-Scheme SnSe₂/Se Heterojunction Photocathode with Enhanced Photoelectrochemical Performance by a Facile One-Step CVD Process, *J. Alloys Compd.*, 2023, **960**, 170985, DOI: **10.1016/j.jallcom.2023.170985**.

14 C. El Haimer, Y. Lghazi, J. Bahar, B. Youbi, M. Ait Himi, A. Ouedrhiri, A. Aynaou and I. Bimaghra, Investigation of Nucleation and Growth Mechanism of Selenium Electrodeposited on ITO Substrate, *Mater. Today: Proc.*, 2022, **66**, 37–44, DOI: **10.1016/j.matpr.2022.03.107**.

15 J. Keller, K. Kiselman, O. Donzel-Gargand, N. M. Martin, M. Babucci, O. Lundberg, E. Wallin, L. Stolt and M. Edoff, High-Concentration Silver Alloying and Steep Back-Contact Gallium Grading Enabling Copper Indium Gallium Selenide Solar Cell with 23.6% Efficiency, *Nat. Energy*, 2024, **9**(4), 467–478, DOI: **10.1038/s41560-024-01472-3**.

16 Y. Gong, Q. Zhu, B. Li, S. Wang, B. Duan, L. Lou, C. Xiang, E. Jedlicka, R. Giridharagopal, Y. Zhou, Q. Dai, W. Yan, S. Chen, Q. Meng and H. Xin, Elemental De-Mixing-Induced Epitaxial Kesterite/CdS Interface Enabling 13%-Efficiency Kesterite Solar Cells, *Nat. Energy*, 2022, **7**(10), 966–977, DOI: **10.1038/s41560-022-01132-4**.

17 Y. Cao, X. Zhu, H. Chen, X. Zhang, J. Zhouc, Z. Hu and J. Pang, Towards High Efficiency Inverted Sb₂Se₃ Thin Film Solar Cells, *Sol. Energy Mater. Sol. Cells*, 2019, **200**, 109945, DOI: **10.1016/j.solmat.2019.109945**.

18 J. Tauc, R. Grigorovici and A. Vancu, Optical Properties and Electronic Structure of Amorphous Germanium, *Phys. Status Solidi B*, 1966, **15**(2), 627–637, DOI: **10.1002/PSSB.19660150224;SUBPAGE:STRING:ABSTRACT;WEBSITE:WEBSITE:PERICLES;JOURNAL:JOURNAL:15213951;REQUESTED JOURNAL:JOURNAL:15213951;WGROUP:STRING:PUBLICATION**.

19 T. Higashi, H. Kaneko, T. Minegishi, H. Kobayashi, M. Zhong, Y. Kuang, T. Hisatomi, M. Katayama, T. Takata, H. Nishiyama, T. Yamada and K. Domen, Overall Water Splitting by Photoelectrochemical Cells Consisting of (ZnSe)₀.₈₅(CuIn₀.₇Ga₀.₃Se₂)₀.₁₅ Photocathodes and BiVO₄ Photoanodes, *Chem. Commun.*, 2017, **53**(85), 11674–11677, DOI: **10.1039/C7CC06637F**.

20 D. Huang, K. Wang, L. Li, K. Feng, N. An, S. Ikeda, Y. Kuang, Y. Ng and F. Jiang, 3.17% Efficient Cu₂ZnSnS₄–BiVO 4 Integrated Tandem Cell for Standalone Overall Solar Water Splitting, *Energy Environ. Sci.*, 2021, **14**(3), 1480–1489, DOI: **10.1039/D0EE03892J**.

21 W. Fuhs, P. Schlotter and J. Stuke, Electrical and Optical Properties of Amorphous and Monoclinic Selenium under Very High Pressure, *Phys. Status Solidi B*, 1973, **57**(2), 587–592, DOI: **10.1002/pssb.2220570215**.

22 J. Li, D. Li, F. Gao, Y. Han, J. Yan and S. Liu, Enabling Solar Hydrogen Production over Selenium: Surface State Passivation and Cocatalyst Decoration, *ACS Sustainable Chem. Eng.*, 2021, **9**(29), 9923–9931, DOI: **10.1021/acssuschemeng.1c03066**.

23 A. H. Pinto, E. R. Leite, E. Longo and E. R. de Camargo, Crystallization at Room Temperature from Amorphous to Trigonal Selenium as a Byproduct of the Synthesis of Water Dispersible Zinc Selenide, *Mater. Lett.*, 2012, **87**, 62–65, DOI: **10.1016/j.matlet.2012.07.067**.

24 A. K. Sinha, A. K. Sasmal, S. K. Mehetor, M. Pradhan and T. Pal, Evolution of Amorphous Selenium Nanoballs in Silicone Oil and Their Solvent Induced Morphological Transformation, *Chem. Commun.*, 2014, **50**(99), 15733–15736, DOI: **10.1039/C4CC08168D**.

25 M. B. Costa, M. A. de Araújo, J. Puigdollers, P. Ortega, T. Andreu, C. Voz, E. Saucedo and L. H. Mascaro, The Influence of Annealing on the Sb Layer in the Synthesis of [001]-Oriented Sb₂Se₃ Film for Photoelectrochemical Hydrogen Gas Generation, *Adv. Funct. Mater.*, 2025, 2506401, DOI: **10.1002/adfm.202506401**.

26 I. Caño, A. Navarro-Güell, E. Maggi, M. Barrio, J.-L. Tamarit, S. Svatek, E. Antolín, S. Yan, E. Barrena, B. Galiana, M. Placidi, J. Puigdollers and E. Saucedo, SbSeI and SbSeBr Micro-Columnar Solar Cells by a Novel High Pressure-Based Synthesis Process, *J. Mater. Chem. A*, 2023, **11**(33), 17616–17627, DOI: **10.1039/D3TA03179A**.

27 M. Lippmann, SULFUR OXIDES (SO X), *Environmental Toxicants*, Wiley, 2020, pp. 927–971, DOI: **10.1002/97811194 38922.ch25**.

28 L. Zhang, Y. Li, C. Li, Q. Chen, Z. Zhen, X. Jiang, M. Zhong, F. Zhang and H. Zhu, Scalable Low-Band-Gap $Sb_2Se_3$ Thin-Film Photocathodes for Efficient Visible–Near-Infrared Solar Hydrogen Evolution, *ACS Nano*, 2017, **11**(12), 12753–12763, DOI: **10.1021/acsnano.7b07512**.

29 Y. He, J. E. Thorne, C. H. Wu, P. Ma, C. Du, Q. Dong, J. Guo and D. Wang, What Limits the Performance of $Ta_3N_5$ for Solar Water Splitting?, *Chem*, 2016, **1**(4), 640–655, DOI: **10.1016/j.chempr.2016.09.006**.

30 A. Delgado, M. F. García-Sánchez, J.-C. M'Peko, A. R. Ruiz-Salvador, G. Rodríguez-Gattorno, Y. Echevarría and F. Fernández-Gutierrez, An Elementary Picture of Dielectric Spectroscopy in Solids: Physical Basis, *J. Chem. Educ.*, 2003, **80**(9), 1062, DOI: **10.1021/ed080p1062**.

31 X. Vendrell, Y. Kubyshin, L. Mestres and J. Llorca, CO Oxidation on Ceria Studied by Electrochemical Impedance Spectroscopy, *ChemCatChem*, 2020, **12**(23), 5926–5931, DOI: **10.1002/CCTC.202001389;REQUESTEDJOURNAL:JOURNAL: 18673899;WGROUP:STRING:PUBLICATION**.

32 T. J. Frankcombe and Y. Liu, Interpretation of Oxygen 1s X-Ray Photoelectron Spectroscopy of ZnO, *Chem. Mater.*, 2023, **35**(14), 5468–5474, DOI: **10.1021/acs.chemmater.3c00801**.

33 R. R. Prabhakar, T. Moehl, S. Siol, J. Suh and D. Tilley, $Sb_2S_3$/$TiO_2$ Heterojunction Photocathodes: Band Alignment and Water Splitting Properties, *Chem. Mater.*, 2020, **32**(17), 7247–7253, DOI: **10.26434/chemrxiv.12110208**.

34 Y.-C. Wang, Y.-Y. Zeng, L.-H. Li, C. Qin, Y.-W. Wang, Z.-R. Lou, F.-Y. Liu, Z.-Z. Ye and L.-P. Zhu, A Stable and Efficient Photocathode Using an $Sb_2S_3$ Absorber in a Near-Neutral Electrolyte for Water Splitting, *ACS Appl. Energy Mater.*, 2020, **3**(7), 6188–6194, DOI: **10.1021/acsaem.0c00210**.

35 G. Liang, Z. Li, M. Ishaq, Z. Zheng, Z. Su, H. Ma, X. Zhang, P. Fan and S. Chen, Charge Separation Enhancement Enables Record Photocurrent Density in $Cu_2ZnSn(S,Se)_4$ Photocathodes for Efficient Solar Hydrogen Production, *Adv. Energy Mater.*, 2023, **13**(19), 2300215, DOI: **10.1002/aenm.202300215**.

36 D. Huang, K. Wang, L. Li, K. Feng, N. An, S. Ikeda, Y. Kuang, Y. Ng and F. Jiang, 3.17% Efficient $Cu_2ZnSnS_4$–$BiVO_4$ Integrated Tandem Cell for Standalone Overall Solar Water Splitting, *Energy Environ. Sci.*, 2021, **14**(3), 1480–1489, DOI: **10.1039/D0EE03892J**.

37 M. Abbas, S. Chen, Z. Li, M. Ishaq, Z. Zheng, J. Hu, Z. Su, Y. Li, L. Ding and G. Liang, Highest Solar-to-Hydrogen Conversion Efficiency in $Cu_2ZnSnS_4$ Photocathodes and Its Directly Unbiased Solar Seawater Splitting, *Nano-Micro Lett.*, 2025, **17**(1), 257, DOI: **10.1007/s40820-025-01755-8**.

38 S. Grau, S. Giraldo, E. Saucedo, J. R. Morante, A. Llobet and C. Gimbert-Suriñach, Multi-Layered Photocathodes Based on $Cu_2ZnSnSe_4$ Absorber and $MoS_2$ Catalyst for the Hydrogen Evolution Reaction, *J. Mater. Chem. A*, 2019, **7**(42), 24320–24327, DOI: **10.1039/C9TA08818K**.

39 C. Ros, T. Andreu, S. Giraldo, V. Izquierdo-Roca, E. Saucedo and J. R. Morante, Turning Earth Abundant Kesterite-Based Solar Cells Into Efficient Protected Water-Splitting Photocathodes, *ACS Appl. Mater. Interfaces*, 2018, **10**(16), 13425–13433, DOI: **10.1021/acsami.8b00062**.

40 M. Chen, Y. Liu, C. Li, A. Li, X. Chang, W. Liu, Y. Sun, T. Wang and J. Gong, Spatial Control of Cocatalysts and Elimination of Interfacial Defects towards Efficient and Robust CIGS Photocathodes for Solar Water Splitting, *Energy Environ. Sci.*, 2018, **11**(8), 2025–2034, DOI: **10.1039/C7EE03650G**.